Unsteady laminar flow developing in a curved duct

M. P. Arnal, D. J. Goering, and J. A. C. Humphrey
Department of Mechanical Engineering, University of California, Berkeley, CA, USA

The flow developing in a tightly curved U-bend of square cross section has been investigated experimentally and via numerical simulation. Both long-time averages and time histories of the longitudinal (streamwise) component of velocity were measured using a laser-Doppler velocimeter. The Reynolds number investigated was Re = 1400. The data were obtained at different bend angles, θ, and were confined to the symmetry plane of the bend. At Re = 1400, the flow entering the bend is steady, but by $\theta = 90°$ it develops an oscillatory component of motion along the outer-radius wall. Autocorrelations and energy spectra derived from the time histories yield a base frequency of approximately 0.1 Hz for these oscillations. Flow-visualization studies showed that the proximity of the outer-radius wall served to damp the amplitude of the spanwise oscillations.

Numerical simulations of the flow were performed using both steady and unsteady versions of the finite-difference elliptic calculation procedure of Humphrey et al. (1977). Although the unsteadiness observed experimentally does not arise spontaneously in the calculations, numerical experiments involving the imposition of a periodic time-dependent perturbation at the inlet plane suggest that the U-bend acts upon the incoming flow so as to damp the amplitude of the imposed oscillation while altering its frequency.

The oscillations observed experimentally, and numerically as a result of the periodic perturbation, have been linked to the formation of Goertler-type vortices on the outer-radius wall in the developing flow. The vortices, which develop as a result of the centrifugal instability of the flow on the outer-radius wall, undergo a further transition to an unsteady regime at higher flow rates.

Keywords: unsteady; laminar; curved duct; Goertler vortices

1. Introduction

In the present study we are concerned with manifestations of instabilities and unsteadiness in the flow developing in a U-bend of square cross section connected to straight tangents up- and downstream of the bend. In such a configuration, one might expect to find that small disturbances develop and grow in the curved section that cannot persist in the straight tangents. This certainly is the situation in curved channels, as shown by Dean (1928a). While the U-bend configuration has been investigated extensively in the fully turbulent regime (Chang et al. 1983; Johnson and Launder 1985), relatively little attention has been given to understanding the evolution of the streamlined motion to time-dependent flow. The only work relating to this point known to us is that by Tsuda and Ohba (1984) and Ohba et al. (1986), discussed below.

By comparison, the investigation of instabilities in fully developed flows in curved ducts is extensive and includes the experimental studies on flow unsteadiness performed by Taylor (1929), the theoretical analyses conducted by Dean (1927, 1928b), and the numerical calculations undertaken by Winters (1987), among others.

Address reprint requests to Dr. Arnal at his present address: ABB Power Generation, Ltd., Dept. KWDT31, CH-5401 Baden, Switzerland.

Received 23 October 1990; accepted 10 March 1992

The analyses by Dean (1927, 1928b) show that the basic solution for the developed laminar motion of the fluid through a curved duct involves a symmetrical pair of counter-rotating vortices, or *cells*, contained in the duct cross section. For fully developed laminar flow in a duct with $R_c/D_h \gg 1$, the dynamical parameter characterizing the secondary motion is the Dean number, $De = Re(D_h/2R_c)^{1/2}$. The Reynolds number is defined as $Re = D_h U_b/\nu$, based on the hydraulic diameter of the duct, D_h, the bulk velocity, U_b, and the fluid kinematic viscosity, ν. The mean radius of curvature of the duct is given by R_c. For developing flows or the fully developed flow in a tightly curved bend, the curvature ratio (R_c/D_h) appears as an additional governing parameter.

Using dye injection for flow visualization, Taylor (1929) studied the laminar–turbulent flow transition in curved pipes. Two important ideas of relevance to the present investigations are suggested by Taylor's observations:

(1) the geometrical symmetry plane of a curved duct or pipe may not necessarily be a flow symmetry plane—Taylor noted that dye injected in one symmetric half of the curved tube occasionally found its way into the other half of the tube cross section;
(2) the streamlined motion through a curved duct or pipe may exhibit large-scale flow unsteadiness of a nonturbulent nature.

Although the unsteadiness in Taylor's experiments was observed close to the point of transition, the possibility that

the flow may be unsteady without being turbulent is suggested.

Theoretical support for these conjectures is contained in the laminar-flow bifurcation studies performed by Winters (1987). For developed flows in curved ducts of square cross section, the author predicts a transition from two cells in a cross section to a different four-cell flow, with the two new cells appearing at the outer curved surface. The transition observed by Winters is the result of a complex structure of multiple, symmetric, and asymmetric solutions that arise from the nonlinearities in the Navier–Stokes equations. Winters (1987) found that all the solutions in the bifurcation diagram for the fully developed flow, except those associated with two-cell branches, were unstable when perturbations that break the axial symmetry were taken into account. His work illustrates the danger of imposing the symmetry of the geometry upon the solution of the flow equations, since such an assumption excludes the possibility of asymmetric, possibly time-periodic flows and may lead to an incomplete solution with incorrect stability properties.

Additional support for the two conjectures drawn from Taylor's observations can be found in the experimental studies by Tsuda and Ohba (1984) and Ohba et al. (1986). Using a laser-Doppler velocimeter, the authors measured bimodal probability density functions and obtained the corresponding spectra for two velocity components in the case of laminar flow developing in a U-bend of square cross section. Regions of alternating high and low streamwise velocity were observed at a bend angle of 90° for Re = 670 and Re = 1340. These values correspond to Dean numbers of De = 153 and De = 307, respectively. The estimated oscillation frequency at the measurement location, which was in the geometrical center of the bend half-plane, was about 3 Hz. However, for Reynolds numbers outside of this range ($Re \leqslant 167$, $Re \geqslant 1500$), the authors did not find any evidence of flow unsteadiness.

Some of the discussion presented in this introduction has been for fully developed flows. The conclusions must be viewed with caution when interpreting developing flows. Taylor's (1929) flow-visualization observations point to the possible presence of non-turbulent oscillations and unsteadiness occurring prior to the laminar–turbulent transition. The experimental data obtained by Tsuda and Ohba (1984), and Winters' (1987) theoretical work, suggest that large-scale unsteadiness may occur in curved-duct flows at intermediate Reynolds numbers, well below the critical value for the onset of turbulence. However, little is known concerning the appearance and role of unsteadiness in developing flows.

There is, therefore, a strong motivation to investigate the question of unsteadiness in developing flows through curved ducts. In the present study, measurements of the time-dependent velocity were obtained using a laser-Doppler velocimeter. Autocorrelations, energy spectra, and probability distribution functions (PDFs) were, in turn, derived from the time records. In addition to the measurements, numerical calculations of the flow have been performed using a three-dimensional (3-D), transient, fully elliptic, finite-difference calculation procedure. Some of the results obtained are presented and discussed here, in an effort to clarify various features of laminar flow developing in a strongly curved duct.

2. The experiment

2.1. Description of experimental apparatus

The experimental apparatus consists of a closed-loop, constant-head water rig that includes the curved-duct test section. A laser-Doppler velocimeter (LDV) with its associated electronic instrumentation and minicomputer were used to obtain measurements of the streamwise velocity component (U_θ). An IBM PC-AT was subsequently employed for additional data analysis and statistical processing. The data-collection system has the capability of calculating mean flow statistics or storing time-dependent data for postprocessing using in-house software on the minicomputer. Both options were used in the present study. The system is essentially the same one described in detail by Chang et al. (1983) and Arnal (1988).

The test section, shown in Figure 1a, consists of a 180° bend and straight-duct tangents, all of which are contained in a vertical plane aligned with the gravity vector. Both the curved duct and tangents have a square cross section. The ratio of the mean radius of curvature to the duct hydraulic diameter is $R_c/D_h = 3.35$. The flow rate can be varied from 2 to 100 liters/min and kept to within 2% of the mean bulk flow rate for several hours, if necessary, so that measurements can be made under constant property conditions. A schematic of the entire apparatus is shown in Figure 2.

Fluid temperature variations during a run remained considerably smaller than 1°C. If they existed in the present configuration, weak buoyancy-driven motions of the type affecting the flow investigated by Hille et al. (1985) did not have a noticeable influence on the results of this study. The governing dimensionless parameter is the Richardson number

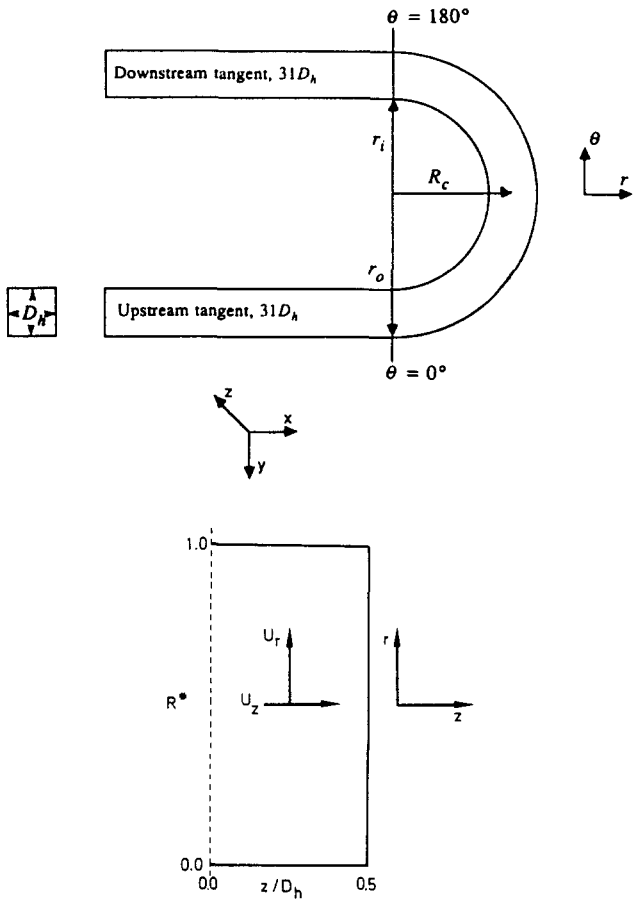

Figure 1 (a) The test section consists of a 180° curved duct of square cross section with straight upstream and downstream tangents attached. The test-section dimensions were D_h = 0.0445 m, R_c = 0.1493 m, r_i = 0.1270 m, and r_o = 0.1715 m. (b) The coordinate system and velocity components employed in the study

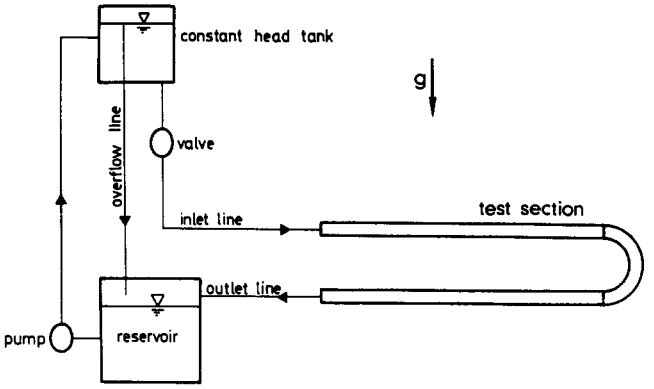

Figure 2 Experimental flow loop showing the constant-head water rig and reservoir, piping, and test section

(Ri), which relates the inertia and buoyancy forces acting on the fluid to produce secondary motion. For small values (Ri < 1), the secondary motion is dominated by the centrifugal forces acting in the bend. For the lowest flow rates investigated in this study (Re = 800, De = 309), the Richardson number was much less than one. At higher flow rates, the buoyancy forces will be even less significant.

2.2. Experimental methodology

2.2.1. LDV measurements. Preliminary flow-visualization experiments were performed to check for the existence of unsteadiness in the vicinity of the curved-duct symmetry plane (Arnal 1988). The visualization study was followed by a series of LDV measurements made in the duct symmetry plane at a Reynolds number of Re = 1400. This was the lowest Reynolds number for which unsteady behavior was observed in the flow-visualization investigations. Radial profiles of the mean streamwise component (U_θ) and RMS velocity were obtained at six streamwise locations in the duct ($x = -5D_h$, $\theta = 3°, 45°, 90°, 135°, 177°$). Each profile consisted of 20 to 25 equally spaced measurement points except in the near wall regions. At each point the mean velocity and RMS values were determined from not less than 2500 individual measurements.

Time histories consisting of 5 to 10 sequences of 250 observations each were taken at selected points in each profile. For the most interesting points, additional time histories were obtained from which the final, mean autocorrelations and spectra were determined. Allowance was made for the nonuniform data rates by using the slotted correlation technique discussed by Bell (1986).

A counter-type processor was used to determine the Doppler frequency. Data rates varied between 10 Hz for the lowest flow rate and more than 100 Hz for the highest flow rate, with an average validation of 60%. The signal-to-noise ratio in most cases exceeded 20 db, except in the near wall regions and at the lowest flow rates.

2.2.2. Experimental uncertainties. There are two ways in which uncertainties due to random and systematic errors show up in the present work. The first is in the data themselves. Statistical quantities such as the mean and RMS velocities are subject to a variety of uncertainties, which have been dealt with in the literature (Drain 1980). A careful estimate of these contributions to the uncertainty in the measurements has been made (Arnal 1988). For the mean-velocity measurements, the combined uncertainty was as large as ±5% in the near wall regions. For the majority of the measurements, away from the duct walls, the uncertainty was estimated to be less than ±2%.

In addition to the uncertainties in the mean flow measurements, there are uncertainties associated with the time sequences from which they are derived. The autocorrelations and power spectra will have upper and lower limits on the frequencies that can be resolved. The highest resolvable frequency is governed by the Nyquist cutoff frequency, which is $1/(2\tau)$, where τ is the time delay chosen to estimate the autocorrelation function; see Bell (1986). In the present study the time delay used was 3 to 10 times greater than the inverse of the average data rate. For the Reynolds number of interest, this yields a maximum resolvable frequency of $\omega_{max} \approx 10$ Hz. The frequency range is bounded on the lower end by the finite length of the time sequences. This corresponds to frequencies on the order of 0.04 Hz for the case investigated. In the present study, the frequencies of interest were well within the band defined by the high- and low-frequency limits.

Within the range of frequencies, the resolution of different frequencies of similar magnitude is also limited by the time delay chosen. Small time delays will lead, in general, to a fine resolution of a narrow frequency band. The final choice of τ in this work has the effect of filtering out high-frequency information content from the data, but it does not alter the qualitative conclusions made concerning the low-frequency range.

3. The numerical procedure

3.1. Conservation equations

The equations describing the incompressible flow in curved ducts of rectangular cross section are the continuity equation and the three momentum equations in cylindrical coordinates. The equations are written here in conservation form for a fluid with constant properties.

Continuity:

$$\frac{1}{r}\frac{\partial}{\partial r}(rU_r) + \frac{1}{r}\frac{\partial}{\partial \theta}(U_\theta) + \frac{\partial}{\partial z}(U_z) = 0 \tag{1}$$

R-momentum:

$$\frac{\partial}{\partial t}(U_r) + \frac{1}{r}\frac{\partial}{\partial r}(rU_rU_r) + \frac{1}{r}\frac{\partial}{\partial \theta}(U_\theta U_r) + \frac{\partial}{\partial z}(U_zU_r) - \frac{U_\theta U_\theta}{r}$$
$$= -\frac{1}{\rho}\frac{\partial p}{\partial r} + \frac{\nu}{r}\frac{\partial}{\partial r}\left(r\frac{\partial U_r}{\partial r}\right) + \frac{\nu}{r}\frac{\partial}{\partial \theta}\left(\frac{1}{r}\frac{\partial U_r}{\partial \theta}\right)$$
$$+ \nu\frac{\partial}{\partial z}\left(\frac{\partial U_r}{\partial z}\right) - \frac{\nu}{r}\left(\frac{U_r}{r} + \frac{2}{r}\frac{\partial U_\theta}{\partial \theta}\right) \tag{2}$$

θ-momentum:

$$\frac{\partial}{\partial t}(U_\theta) + \frac{1}{r}\frac{\partial}{\partial r}(rU_rU_\theta) + \frac{1}{r}\frac{\partial}{\partial \theta}(U_\theta U_\theta) + \frac{\partial}{\partial z}(U_zU_\theta) + \frac{U_rU_\theta}{r}$$
$$= -\frac{1}{\rho r}\frac{\partial p}{\partial \theta} + \frac{\nu}{r}\frac{\partial}{\partial r}\left(r\frac{\partial U_\theta}{\partial r}\right) + \frac{\nu}{r}\frac{\partial}{\partial \theta}\left(\frac{1}{r}\frac{\partial U_\theta}{\partial \theta}\right)$$
$$+ \nu\frac{\partial}{\partial z}\left(\frac{\partial U_\theta}{\partial z}\right) - \frac{\nu}{r}\left(\frac{U_\theta}{r} - \frac{2}{r}\frac{\partial U_r}{\partial \theta}\right) \tag{3}$$

z-momentum:

$$\frac{\partial}{\partial t}(U_z) + \frac{1}{r}\frac{\partial}{\partial r}(rU_rU_z) + \frac{1}{r}\frac{\partial}{\partial \theta}(U_\theta U_z) + \frac{\partial}{\partial z}(U_zU_z)$$
$$= -\frac{1}{\rho}\frac{\partial p}{\partial z} + \frac{\nu}{r}\frac{\partial}{\partial r}\left(r\frac{\partial U_z}{\partial r}\right) + \frac{\nu}{r}\frac{\partial}{\partial \theta}\left(\frac{1}{r}\frac{\partial U_z}{\partial \theta}\right) + \nu\frac{\partial}{\partial z}\left(\frac{\partial U_z}{\partial z}\right) \tag{4}$$

In the above equations, U_r, U_θ, U_z are the three velocity components in the radial, streamwise, and cross-stream (axial) directions, respectively. The pressure is denoted by p, and the fluid density by ρ, and ν represents the kinematic viscosity. The coordinate system and velocity components employed in the study are illustrated in Figure 1a and b. Note that the dimensionless radial coordinate is defined as $R^* = (r - r_i)/(r_o - r_i)$.

3.2. Boundary conditions

At the inlet to the curved duct ($\theta = 0°$), the velocity profile was specified. For the cases presented in this study, a fully developed straight-duct profile was used. The deviations from this symmetric profile that occur experimentally are small except in cases of very strong curvature.

Some of the unsteady calculations discussed in Section 4 were perturbed by introducing a harmonic, time-dependent pulsation to the streamwise velocity at the inlet plane. In these calculations, the base fully developed profile was pulsed by $\pm 2.5\%$ on each side of the duct symmetry plane. The perturbation was harmonic in time with a phase shift of 180° between the right and the left half of the inlet plane. This phase shift allowed the bulk flow rate to remain constant at all times.

At the outlet plane ($\theta = 180°$), the velocities were linearly extrapolated. This is equivalent to requiring that the second derivative of the velocity by zero in the streamwise direction ($\partial^2\phi/\partial\theta^2 = 0$). This condition allows the flow to continue developing at the outlet, unlike a constant extrapolation condition ($\partial\phi/\partial\theta = 0$). As a result, the linearly extrapolated outlet condition exerts much less of an influence on the flow field upstream of the outlet plane. This was particularly noticeable in the time-dependent calculations, where wavy structures were free to flow out of the computational domain.

Conditions of impermeability and no-slip were used to specify the velocity components at the solid duct walls. Finally, a no-shear condition was used at the geometric symmetry plane ($z/D_h = 0$) for those cases in which the full duct cross section was not calculated.

3.3. Solution methodology

The finite-difference form of the governing equations is obtained by integrating Equations 1 to 4 over a control volume of the computational mesh. The Hybrid differencing scheme due to Spalding (1972) was used for the discretization of the convective terms. The diffusive terms are discretized using the central differencing scheme. A first-order, fully implicit forward Euler scheme was used to discretize the time-dependent terms.

A finite-volume method with a staggered variable arrangement is used for solving the resulting system of equations. The pressure and velocity fields are coupled in the iterative SIMPLER (SIMPLE-Revised) algorithm due to Patankar (1981). The linearized system of equations arising from the discretization procedure is solved using the modified strongly implicit (MSI) procedure of Schneider and Zedan (1981). The MSI procedure is an iterative solution method based on the earlier strongly implicit procedure of Stone (1968). The convergence rate of the numerical procedure was accelerated by employing a downstream bulk-pressure correction as suggested by Pratap (1975). This has the effect of more strongly linking the pressure field at each plane to neighboring planes in the streamwise direction.

3.4. Testing

The test cases consisted of steady developing laminar flow in a 90° curved duct (for spatial resolution) and 2-D unsteady laminar flow past a square cylinder (for temporal accuracy).

3.4.1. Spatial grid refinement. As a result of using the Hybrid differencing scheme in the present calculations, upwind differencing is used in regions where convection dominates. Because of the first-order accuracy of the upwind scheme, numerical diffusion is a potential problem. The test case chosen for the grid-dependence study was the steady flow through a 90° bend with a square cross section and a radius of curvature ratio of $R_c/D_h = 2.3$, as investigated by Humphrey (1977). Calculations were made assuming a steady-state solution, so that the unsteady terms in Equations 2 to 4 were set to zero. Several different runs were made with both uniform and nonuniform node distributions in the streamwise and cross-stream directions.

Based on the results of the grid-refinement study, a nonuniform (z, r, θ) grid of $(30 \times 30 \times 45)$ was chosen for the calculations of the 180° bend with the full cross section considered. This degree of grid refinement represents a compromise between an adequate resolution of the flow field (in particular, the side-wall boundary layers) and affordable calculations. With this grid, the maximum error in the velocity profiles (U_θ, U_r) was estimated to be 6% of the reference velocity, U_b. The maximum error in the shear stress was estimated to be 2% of the reference value, $\frac{1}{2}\rho U_b^2$. The maximum discrepancies occur in the first 30° of the duct.

3.4.2. Temporal grid refinement. A 2-D version of the present numerical procedure was used to investigate the influence of time-step size on the numerical results. The test case concerned the simulation of vortex shedding from a square rib in a freestream flow at a Reynolds number of Re = 500. The characteristic time scale in this flow is given by the rib dimension divided by the freestream fluid velocity. Calculations were carried out in which the flow was started impulsively using nondimensional time-step sizes of 0.1 and 0.025. Periodic vortex shedding developed after approximately 20 time scales of elapsed time. The frequency of vortex shedding was compared with the results of two experimental studies in the literature. Although there is significant scatter in the two data sets, the numerical results obtained with the present numerical procedure agreed with each to within 10%. The predicted shedding frequency varied by only 3% when the time-step size was refined.

The results discussed above offer guidance in choosing appropriate time-step sizes for the unsteady curved-duct flow simulations. These calculations, to be discussed in Section 4, were performed with time-step sizes on the order of 0.1 of the shortest characteristic time scale, D_h/U_b, present in the flow.

All the calculations discussed in the present study were performed on the Cray X-MP of the University of California, Berkeley. Typical convergence times for the steady-flow calculations were 30 to 45 minutes for a total of 300 to 450 iterations. For the time-dependent calculations, approximately 10 to 15 minutes of computer time was needed per flow time-scale (D_h/U_b) in the simulation.

4. Results

In this section, both mean (long-time averaged) and time-dependent experimental results are presented and compared with steady and unsteady predictions of the flow field. The flow in the bend at a Reynolds number of Re = 1400 is the focus of both the experimental and numerical studies. This Reynolds number corresponds to the lowest value for which flow unsteadiness was observed in the flow-visualization experiments. For the given bend geometry, this corresponds to a Dean number of De = 541.

The predictions made assuming steady-state behavior are first compared with the measurements of the mean, streamwise (U_θ) velocity component. The calculations were made by setting the time-dependent terms in Equations 2 to 4 to zero and seeking a solution to the resulting steady-state equations. After comparing the predicted and measured profiles of the U_θ-velocity, a further discussion of the predicted steady-state flow field is given. Following this, the results of the time-dependent measurements are presented and compared qualitatively with the results of calculations made with the time-dependent version of the numerical procedure.

4.1. The mean flow field

4.1.1. Comparison of measurements and predictions. The measured and predicted values of the U_θ-profile on the bend symmetry plane are compared in Figure 3. The calculations were made considering one symmetric half of the duct cross section with a zero-gradient boundary condition imposed for U_θ and U_r and with $U_z = 0$ at the symmetry plane of the bend. The fully developed profile for the flow through a straight duct with a square cross section was used as the inlet profile for the curved duct (0° plane). This profile is compared with the measured profile at $2.5D_h$ upstream of the bend at the bottom of Figure 3. As explained by Humphrey et al. (1977), the flow in this region is slightly altered by the bend through the elliptic influence of the pressure field. However, the influence of the bend on the upstream tangent flow does not extend significantly beyond this point.

At 3° into the duct, there is a clear departure from the flow symmetry in the radial direction. The predictions barely show the characteristic swing towards r_i exhibited in the measurements. This shift in the U_θ-profile is due to a favorable streamwise pressure gradient that exists at the inner-radius wall in the inlet region of the bend.

At the 45°, 90°, and 135° planes, the influence of the cross-stream secondary motion on the measured U_θ profile is quite evident. The secondary flow displaces fluid with high streamwise momentum from the outer-radius wall region along the side walls towards the inner-radius wall. At the same time, the fluid with low streamwise momentum near the inner-radius wall is displaced along the symmetry plane into the core of the flow. This accounts for the local minimum observed at each of these three streamwise positions. This effect of the secondary flow is also reproduced in the predictions, although the correct location of the velocity minima is only reproduced after the 90° plane. It appears that, partly as a result of differences between the measured and imposed inlet conditions, the development of the predicted flow field lags somewhat behind the measurements in the first half of the bend (e.g., 45° and 90° planes). This effect may also be partly due to an insufficient resolution of the side-wall boundary layers.

Downstream of the 90° plane, the agreement between the experiments and predictions is much better. The prediction of the magnitude and location of the velocity maximum agrees well with the measured values. The imposed outlet boundary condition proved to be sufficiently accurate to permit an overall correct flow development in the bend. In contrast, earlier calculations assuming fully developed flow at the outlet led to excessive smoothing of the flow field in this region. At the 135° and 177° planes, the maximum discrepancy between the measured and predicted mean velocities was 5% of the average velocity near r_o.

Measurements of the RMS velocity were also made for the streamwise velocity component at each streamwise location. The measured RMS velocities were almost always very low, usually less than 2% of the bulk velocity. However, near the outer-radius wall at the 135° and 177° planes, the RMS velocities were on the order of 0.15 U_b. These unexpectedly high values are an indication of significant fluctuations about the mean. For the given Reynolds number (which is well below the critical value for transition), these fluctuations are likely to be nonturbulent in nature. Further discussion of these oscillations is given below in relation to the flow unsteadiness.

In comparing the predicted and measured mean-velocity profiles in the bend flow, the maximum discrepancies between the two amounted to 15% of the average velocity. These discrepancies occurred immediately downstream of the bend inlet plane and, as suggested earlier, are likely due to an insufficient resolution of the side-wall boundary layers as well as differences in the measured and specified inlet conditions.

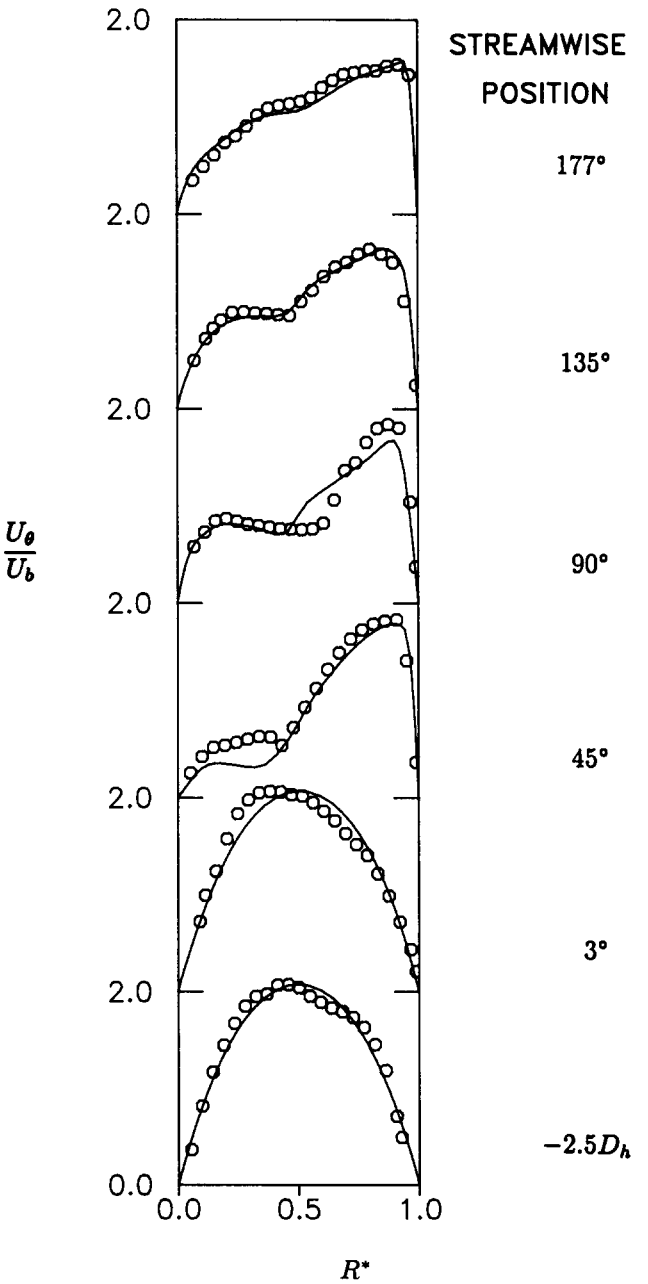

Figure 3 Radial profiles of U_θ/U_b for steady laminar flow in a 180° curved duct, Re = 1400. Velocity profiles on the duct symmetry plane, $z/D_h = 0$

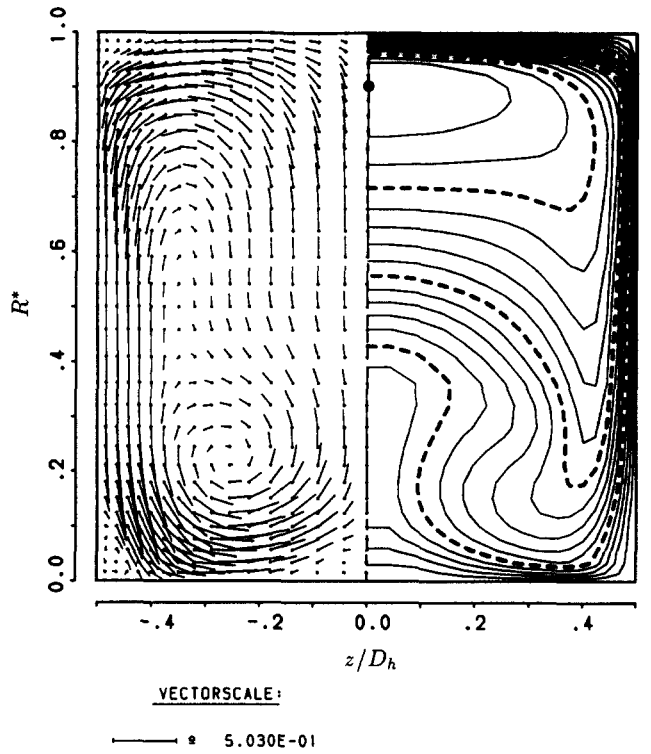

Figure 4 Cross-stream velocity (U_r/U_b, U_z/U_b) vectors and streamwise velocity (U_θ/U_b) contours for steady laminar flow in a 180° curved duct, Re = 1400, $\theta = 45°$. Contours: minimum = 0.00, increment = 0.100, maximum (●) = 1.79, (---): $U_\theta/U_b = 0.5$, 1.0, and 1.5

Predictions of the flow including a portion of the upstream tangent can be expected to be in better agreement with the measured profiles, since the inlet condition would then more accurately represent the experimental case. Downstream of the inlet region, differences between the measured and predicted profiles may be connected with the unsteadiness observed in the experimental study.

4.1.2. Predictions. The comparison of experiments and calculations indicates that the numerical procedure is capable of reproducing the average characteristics of laminar flow developing in a curved duct. In this section, results of the steady-state calculations are examined for evidence of spatial waviness, indicating the potential for unsteady behavior in a time-dependent flow. The availability of the entire 3-D flow field makes such an investigation much easier to perform than would be the case with experimental data alone. In Figures 4 and 5, the predicted cross-stream and streamwise velocity fields are shown for the $\theta = 45°$ and 135° planes of this flow. Cross-stream velocities (U_r, U_z) are shown in the form of a vector plot, and the streamwise velocity (U_θ) is plotted in contours.

At the 45° plane (Figure 4), the cross-stream secondary motion is already well established and has influenced the U_θ contours dramatically. The flow-visualization observations confirmed the existence of the large vortex core located near the inner-radius wall ($z/D_h = \pm 0.25$, $R^* \approx 0.2$). Near the outer-radius wall, there are no additional vortices, and a standard stagnation-type flow occurs in this region.

Figure 5 shows the calculated velocity field for the 135° plane. It was at this position that the experimental study showed the first signs of flow unsteadiness near r_o, as discussed in the following section. Recall that the measured RMS velocities were also unexpectedly high in this region. The presence of two vortices can be noted near r_o in the predictions, which, together with the main core vortex, gives a total of six vortices in the full cross section. There is a distinct spanwise (z-direction) waviness in the streamwise velocity contours shown in the right-hand side of the figure. The vortices near the outer wall arise due to a centrifugal-force–pressure-gradient instability in the boundary layer on the outer-radius wall (Arnal 1988). The development of these vortices is similar to that of the Goertler vortices, which grow in a boundary layer developing on a concave wall. At positions further downstream, the Goertler-type vortices grow larger and stronger and significantly alter the streamwise velocity contours.

4.2. Flow unsteadiness

4.2.1. Measurements. In this section, the results of the unsteady measurements made principally at the $\theta = 135°$ plane are presented. For comparison purposes, all the data have been normalized using a characteristic time ($T_c = D_h/U_b$), length (D_h), and velocity (U_b), where appropriate. Nondimensional frequencies are defined as $\omega = \omega_m D_h/U_b$ where ω_m is the measured frequency in Hz.

The flow-visualization studies first showed evidence of unsteadiness at a Reynolds number of Re = 1400, particularly in the last 60° of the bend near r_o. Figure 6 shows typical time histories taken at the six streamwise measurement stations in the test section for this flow rate. In each case, the measurements were made near the outer-radius wall (r_o) on the duct symmetry plane ($R^* = 0.95$, $z/D_h = 0$). The figure shows a dramatic development in the velocity fluctuations that occur near the

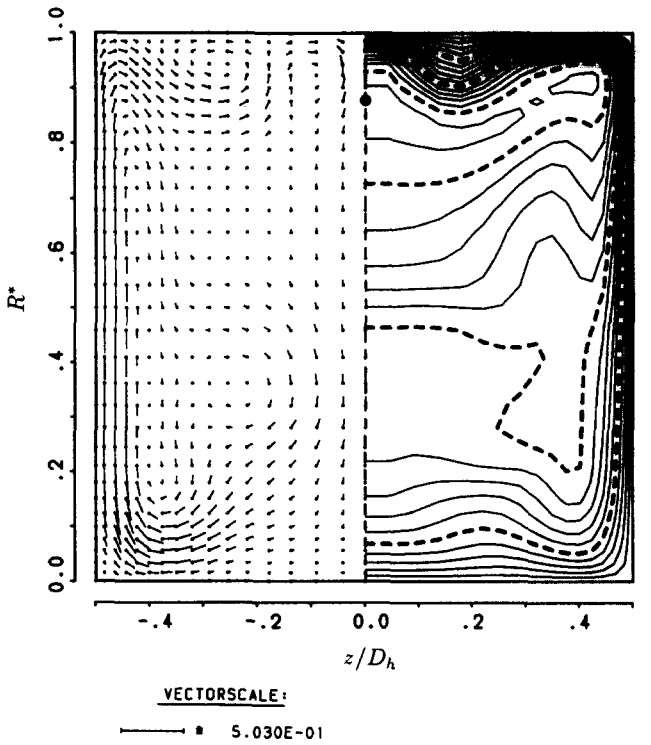

Figure 5 Cross-stream velocity U_r/U_b, U_z/U_b) vectors and streamwise velocity (U_θ/U_b) contours for steady laminar flow in a 180° curved duct, Re = 1400, $\theta = 135°$. Contours: minimum = 0.00, increment = 0.100, maximum (●) = 1.64, (---): $U_\theta/U_b = 0.5$, 1.0, and 1.5

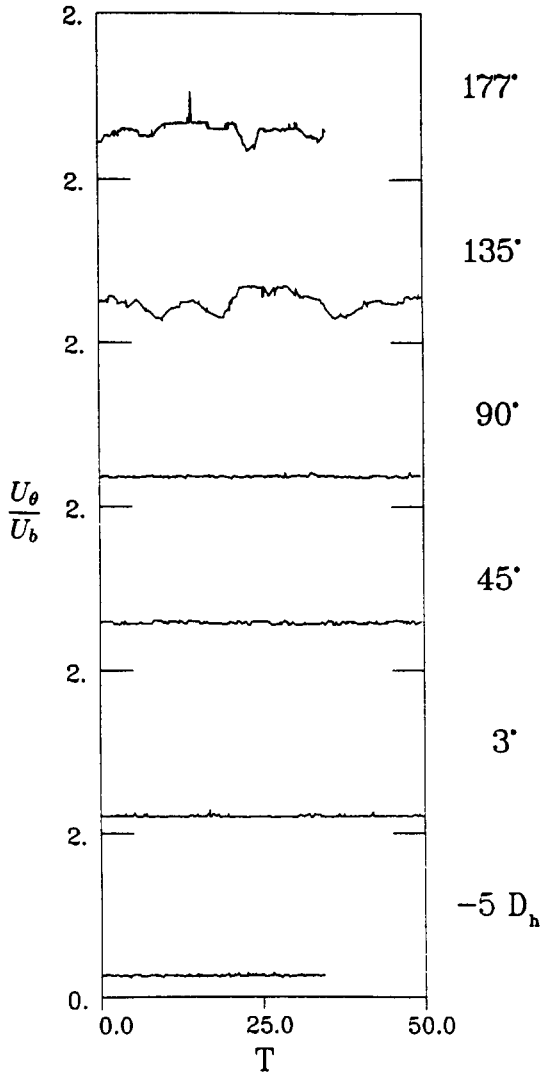

Figure 6 Time variation of the streamwise velocity component as a function of streamwise location for Re = 1400. Measurements made on the duct symmetry plane near r_o ($R^* = 0.95$)

outer-radius wall. Upstream of the bend and through the first 90°, the velocity at this radial position remains very steady. Somewhere between 90° and 135°, large-scale, low-frequency fluctuations develop that persist up to the bend outlet. The time histories at $\theta = 135°$ show quantitatively what was observed qualitatively with the flow-visualization studies. Large-scale fluctuations about the mean are clearly visible. A similar series of time histories was measured near the inner-radius wall, r_i, which showed no large-scale fluctuations about the mean, again in agreement with the flow-visualization studies.

Further measurement effort focused on the $\theta = 135°$ plane at radial positions near the outer-radius wall, where additional detailed time histories were obtained. Probability density functions (PDFs), autocorrelations, and energy spectra determined from this data are based on 8,000 to 16,000 individual measurements. Figures 7 to 9 present the average energy spectra for three radial locations near r_o ($R^* = 0.92$, 0.95, 0.98). The corresponding autocorrelations and time series are discussed in detail in Arnal (1988).

Figure 7 corresponds to the position farthest from the outer-radius wall ($R^* = 0.92$). The energy spectrum is dominated at low nondimensional frequencies by a plateau region in the range of $0.06 < \omega < 0.2$. In the time records, oscillations with periods of $2 < T < 14$ ($0.07 < \omega < 0.5$) were also identified. Within the plateau region, two frequencies (ω_1 and ω_2) are shown in the figure. The lower frequency has been singled out because of its dominant role at the radial position closer to the outer-radius wall ($R^* = 0.95$). Note that because of limitations on the total length of the time records, the very-low-frequency portion of the spectrum ($\omega < 0.1$) should be considered with care. Although more than 60 time records were used to obtain this result, the number of samples contributing to the low-frequency range was small.

The fundamental frequencies lead to higher-order harmonics, which are also illustrated in Figure 7. The energy content of these peaks decreases rapidly with increasing frequency. At nondimensional frequencies greater than $\omega = 1$, the energy content is an order of magnitude smaller than the value for the plateau region. Notice that the energy level does not fall to zero at higher frequencies, as might be expected in an unsteady laminar flow. At these frequencies, the energy level is determined by the fluctuations in the data rate and LDV signal.

Of the three positions investigated, the largest mean velocity ($U/U_b = 1.36$) and RMS velocity were observed at this location ($R^* = 0.92$). Low-frequency oscillations were clearly visible in

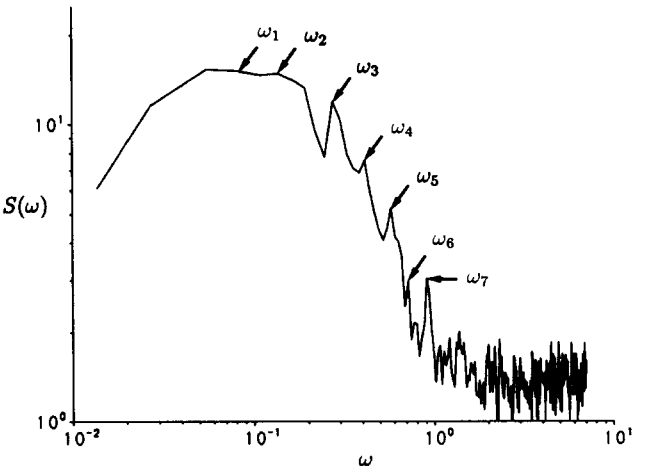

Figure 7 Energy spectrum at $R^* = 0.92$, $\theta = 135°$, $z/D_h = 0.0$

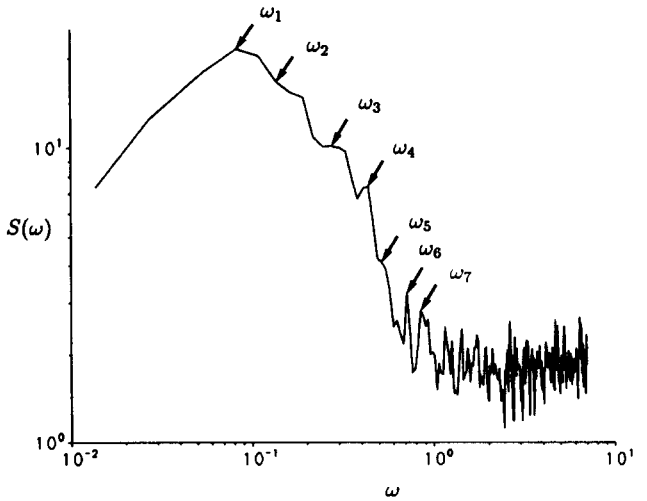

Figure 8 Energy spectrum at $R^* = 0.95$, $\theta = 135°$, $z/D_h = 0.0$

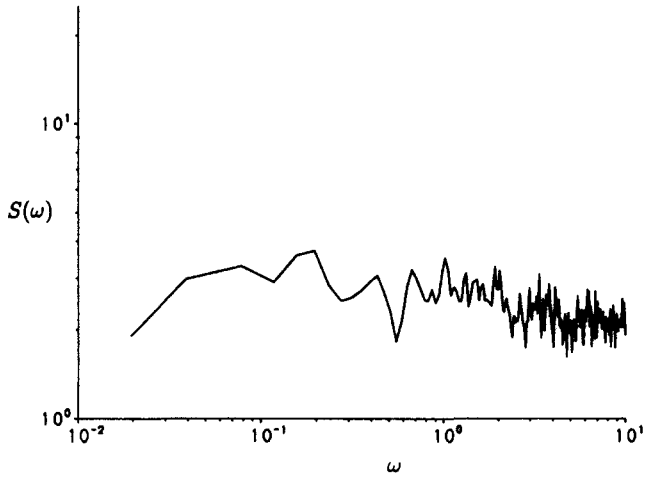

Figure 9 Energy spectrum at $R^* = 0.98$, $\theta = 135°$, $z/D_h = 0.0$

the velocity time records (Arnal 1988). An integral time scale can be defined from the autocorrelation function giving an estimate of the average time during which the fluctuating velocity remains correlated with itself. In the present study the integral time scale was determined for each of the radial positions as

$$T_I = \int_0^\infty \rho(\tau)\, d\tau \tag{5}$$

where $\rho(\tau)$ is the autocorrelation function for the fluctuating velocity, u'_θ. For the position $R^* = 0.92$, the time scale calculated was $T_I = 0.47$, indicating that the velocity remains correlated with itself about half as long as it takes the mean flow to move one hydraulic diameter through the duct.

Figure 8 illustrates the energy spectrum for the position $R^* = 0.95$. As at the previous radial position, the energy spectrum at this location also indicates the presence of low-frequency oscillations in the flow. The spectrum is dominated at low frequencies by a peak, $\omega_1 = 0.085$, which is 15 times larger than the background energy levels at higher frequencies. This fundamental frequency was just one of many occurring in the low-frequency plateau region at the previous radial position, $R^* = 0.92$. The second fundamental frequency (ω_2) shown in Figure 7 is also marked in Figure 8 for comparison. The energy level at this frequency is approximately the same at the two radial positions. The spectrum illustrates the presence of several high-frequency harmonics that also occurred at the radial position further from r_o.

The closer proximity of the curved wall at this position has two noticeable effects on the flow. In comparison with the previous location, the mean velocity is lower ($U/U_b = 0.95$), and the deviations from the local mean are smaller. The outer-radius wall has the effect of decreasing the mean velocity and damping the oscillations about the mean. This stronger influence of the curved wall can also be seen in the integral time scale calculated for this location. The autocorrelation function yields a correlation time scale of $T_I = 0.61$ in nondimensional units, about 20% longer than at the previous location, $R^* = 0.92$. At the position closer to the wall, the oscillations are correlated longer on average, indicating that the structures in this region persist longer.

The harmonics and their equivalents in terms of the base frequencies are summarized for both radial positions in Table 1. Note that the same frequencies appear as harmonics of the base frequencies at the two radial measurement positions. This should be the case if the source of the fluctuations is the same at both radial positions.

At the location closest to r_o ($R^* = 0.98$), the curved wall has an even stronger influence on the flow behavior. The oscillations observed at the other radial positions are completely damped out by the viscous action in this region. The velocity distribution is confined to a very narrow range, and the fluctuations that occurred showed no organized pattern.

The corresponding energy spectrum is shown in Figure 9. The integral time scale calculated for this position was $T_I = 0.08$, less than 20% of the values at locations further from the wall. At a position where oscillations are completely damped out, one would expect a large correlation time. Recall, however, that the LDV measurements contain small random deviations from the mean (fluctuations) due to noise even in a steady flow. The very short integral correlation time at this location ($T_I = 0.08$) is merely a confirmation that the signal fluctuations about the mean velocity are random in nature.

4.2.2. Predictions. To help understand the unsteady behavior of the flow field that is observed experimentally at the 135° plane for Re = 1400, several time-dependent numerical simulations were performed. The flow-visualization studies suggested that the unsteadiness observed at this plane involves flow structures that meander across the symmetry plane of the duct. For this reason, in contrast to the calculations discussed earlier, the symmetry-plane boundary condition was not used. Instead, the flow field in the entire duct cross section was computed. The unsteady calculations were all performed with a nondimensional time-step size of 0.1, in terms of the characteristic flow time, $T_c = D_h/U_b$.

Time-dependent calculations were performed with a variety of initial conditions, both symmetric and asymmetric. In all cases, the simulations resulted in an initial transient period during which the flow readjusted in response to the perturbation. After the transient portion of the simulation, the flow reached a steady state and remained so until the simulations were terminated.

The simulations involving spatial perturbations of the initial flow field produced unsteady behavior of a transient nature. The experimental results, on the other hand, indicate long-term unsteady behavior of the flow field at Re = 1400. In an effort to produce long-term unsteadiness numerically, a time-dependent perturbation was employed at the inlet. The inlet profile at $\theta = 0°$ was specified as follows:

$$U_\theta = \begin{cases} U_{fd}(1 + 0.025\sin(\pi T)) & \text{for } \dfrac{z}{D_h} > 0 \\ U_{fd}(1 - 0.025\sin(\pi T)) & \text{for } \dfrac{z}{D_h} < 0 \end{cases} \tag{6}$$

where U_{fd} is the fully developed, straight-duct velocity and T

Table 1 Observed frequencies for measurement positions: $R^* = 0.92$, 0.95, and $\theta = 135°$

Peak	Frequency	Equivalence	Meas. freq. (Hz)
ω_1	0.09		0.058
ω_2	0.14		0.103
ω_3	0.27	$3\omega_1$, $2\omega_2$	0.195
ω_4	0.44	$5\omega_1$, $3\omega_2$	0.313
ω_5	0.58	$4\omega_2$	0.415
ω_6	0.71	$8\omega_1$, $5\omega_2$	0.506
ω_7	0.9	$10\omega_1$	0.605

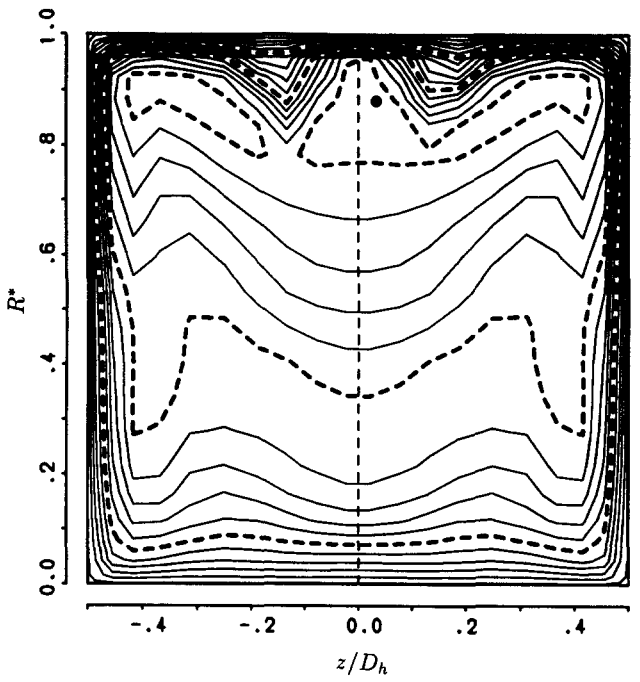

Figure 10 Streamwise velocity (U_θ/U_b) contours for unsteady laminar flow in a 180° curved duct, Re = 1400, θ = 135°, T = 26. Contours: minimum = 0.00, increment = 0.100, maximum (●) = 1.58, (---): U_θ/U_b = 0.5, 1.0, and 1.5

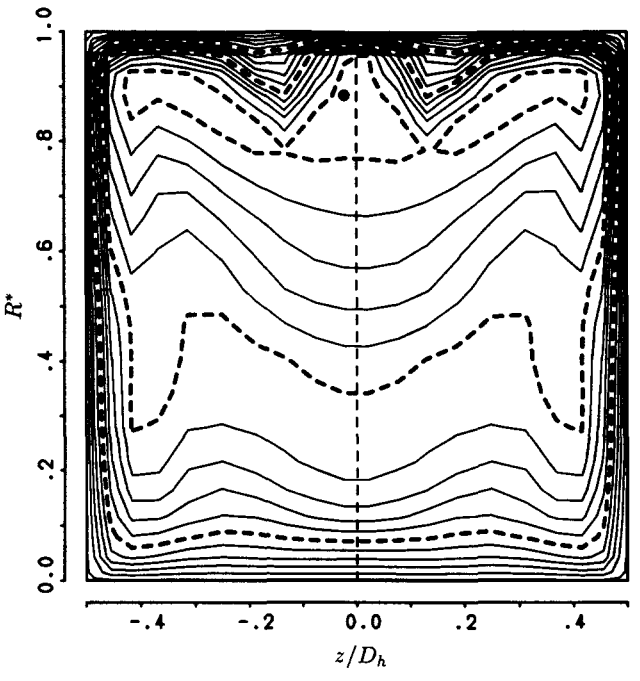

Figure 11 Streamwise velocity (U_θ/U_b) contours for unsteady laminar flow in a 180° curved duct, Re = 1400, θ = 135°, T = 36. Contours: minimum = 0.00, increment = 0.100, maximum (●) = 1.58, (---): U_θ/U_b = 0.5, 1.0, and 1.5

is the dimensionless time. Note that the time-dependent perturbation has an amplitude of 2.5%, is harmonic with a frequency of 0.5 and period of 2.0, and is asymmetric with respect to the symmetry plane of the duct.

Time integration proceeded from an initial condition consisting of the steady-state flow solution for Re = 1400 and was terminated at T = 42 due to mounting computational costs. This time-dependent perturbation produced results that appear to have persistent, long-term unsteady characteristics. Figures 10 and 11 show streamwise velocity (U_θ) contours at the 135° plane for the two extremes in the oscillating flow. The figures reveal a time-dependent asymmetric behavior in the region near the centerline at the outer radius of the bend.

The flow in this region was symmetric for the first 20 time scales of simulation. Accounting for the spiraling motion of the flow, this is the time required for the perturbations imposed at the inlet to reach this plane. During the next six time-scales of simulation, the predicted flow becomes increasingly asymmetric at the θ = 135° plane (Figure 10). Notice that the cross-stream fingers of slow-moving fluid that are generated by the Goertler-type vortices near r_o are asymmetric about the z/D_h = 0 plane. The left-hand vortex pair has moved towards this plane and appears momentarily stronger than the right-hand pair in the figure.

A smaller leftward displacement of the U_θ velocity was observed in the simulation between T = 34 and T = 39. This asymmetry in the U_θ contours illustrated in Figure 11 is also caused by variations in the relative strength of the Goertler-type vortex pairs, although in this case the asymmetry is weaker. After the flow returned to a symmetric state at T = 39–40, it remained symmetric until the simulation was terminated at T = 42.

5. Discussion

5.1. Stabilizing influences in the simulations

As noted earlier, fully converged solutions were obtained for the developing flow in a 180° bend using the steady-state calculation procedure and a symmetry boundary condition at the duct symmetry plane. However, the experimental measurements indicate that the flow is unsteady with flow oscillations occurring near r_o. There are several possibilities as to why a stable, converged, steady solution could be obtained for an unsteady flow. Potential stabilizing factors include

(1) the assumed symmetry-plane boundary condition, which prevents asymmetric solutions from occurring;
(2) numerical diffusion (with the same effect), which depends on the combination of discretization scheme and grid refinement used; or
(3) the neglecting of the time-dependent terms in the momentum equations, which per se prevents temporal perturbations from influencing the flow.

Each of these factors is considered briefly below.

5.1.1. Symmetry-plane assumption. Recent experimental studies by Hille et al. (1985) and theoretical work of Winters (1987), Goering (1989), and Jayanti (1990) have called into question the validity of the symmetry-plane assumption in curved-duct flows. By performing long-time averages on the velocity data obtained in a 180° curved duct, Hille et al. (1985) report an apparently stable, asymmetric distribution of four vortices in the 136° cross-stream plane. Jayanti (1990) discusses the prediction of similar flow patterns that were obtained at the exit plane of a 180° bend. Winters (1987) and Goering (1989) showed numerically that the four-vortex solution that can occur in fully developed curved duct flows is unstable to asymmetric as well as to symmetric perturbations. This means that in calculations with a symmetry plane imposed, unstable

flows could be predicted as stable ones or stable asymmetric solutions would be missed.

In performing the calculations in which steady-state behavior was assumed, the influence of the symmetry plane on the predictions was investigated. Simulations of the bend flow with varying curvature ratios ($1 < R_c/D_h < 12.9$) and Reynolds numbers ($50 < \mathrm{Re} < 2000$) were performed, both with and without the symmetry-plane condition imposed on the flow. In every case, the steady-state calculations yielded symmetric results whether or not the symmetry-plane condition was employed. This is in stark contrast with the results of our calculations as well as with those of Sankar et al. (1988) for the curved-duct flow far downstream of the inlet region. In the latter case, the transition from a four-vertex to a two-vortex solution occurs via a symmetry-breaking three-vortex solution (Arnal 1988). Asymmetric flow patterns were observed far downstream of the inlet region ($\theta > 360°$) for the tightly curved bend considered in the present study. This transition could only occur in calculations considering the full duct cross section.

What distinguishes the flow in the developing region of a curved duct from the corresponding fully developed flow is the presence of large gradients in the streamwise direction. These gradients provide an additional constraint on the developing flow that is not present in the fully developed case. In addition to the no-slip boundary conditions at the duct walls, the upstream inlet flow provides an additional boundary condition in the third (streamwise) coordinate direction. For the fully-developed flow case, the velocity field no longer varies with the streamwise coordinate, so there is no need for boundary conditions in this direction. It would appear that the large streamwise gradients present in the developing region of a curved duct act to stabilize the flow so that only symmetric flow fields are predicted given a symmetric inlet condition. It is well known that accelerating a turbulent (time-dependent) flow acts to stabilize it and, in extreme cases, to lead to flow relaminarization. A similar stabilizing effect of the streamwise gradients seems to occur in the developing flow in a curved duct.

Note that the extent of this development region (where the gradients in the θ-direction are significant) will depend on the Reynolds number and bend-curvature ratio. In general, the development region will be longer for higher values of Re and smaller curvature ratios.

5.1.2. Numerical diffusion. Jayanti (1990) showed that the appearance of an asymmetric flow pattern is very sensitive to the numerical accuracy of the difference schemes used for the convective terms in the governing equations. For example, asymmetries developed at the exit plane of a 180° bend ($\mathrm{Re} > 1100$, $R_c/D_h \geqslant 5$) when the more accurate QUICK scheme was employed. However, only symmetric patterns were observed in similar calculations using the Hybrid scheme, which is also employed in the present study. Numerical diffusion also appears to stabilize symmetric cross-stream flow solutions and to prevent asymmetric solutions from occurring, even in regions where the gradients in the streamwise direction are small.

5.1.3. Temporal gradient terms. A third possibility is that the vortices predicted with the steady-state version of the code are unstable to temporal perturbations. Including the unsteady terms would allow the vortices to move and asymmetries to occur. In the present calculations, recall that time-varying flow of a long-term nature only occurred when a time-dependent perturbation was implemented at the bend inlet.

Of course, it is likely that a combination of the above factors acts to stabilize the steady-state calculations. Of the three factors, only numerical diffusion will adversely influence unsteady calculations based on the full duct cross section. In order to determine to what extent the unsteady calculations are so influenced, further calculations with refined grids or a more accurate differencing scheme would be necessary.

5.2. Flow unsteadiness

The flow characteristics produced by the simulation are in qualitative agreement with the experimental observations. Although it is difficult to assign a frequency to the predicted asymmetric flow variations, it appears that they occur at a frequency on the order of $\omega = 0.05$–0.1. Table 1 shows that the fundamental frequency observed in the LDV data was approximately 0.1. The onset of unsteady behavior in the predictions occurs in a region adjacent to the symmetry line near r_o, where unsteadiness first appeared in the experimental study. We also note that the motion of the Goertler-type vortices, which occurs in the simulation, would induce a fluttering motion similar to that observed in the flow-visualization study discussed in Arnal (1988).

Perhaps the largest discrepancy between the simulation and the experimental observations concerns the amplitude of the observed fluctuations. In the experimental study there were streamwise velocity fluctuations at the symmetry line on the order of 50% of the time-averaged value. The magnitude of the fluctuations in the predictions are much smaller than those observed experimentally. The small amplitudes observed in the simulations could be a result of damping due to numerical diffusion. Further calculations with refined grids or higher-order differencing schemes would be necessary to determine to what extent this is the case.

One of the interesting results of the time-dependent simulations was that the frequency of the imposed perturbation ($\omega_{in} = 0.5$) is much higher than that at which the computed flow asymmetries occur ($0.05 < \omega < 0.1$). The temporal perturbations with a fixed frequency act to disturb the flow in a fashion similar to the random temporal perturbations that occur in the experiment in the upstream tangent. From the present limited time-resolution of the flow ($T < 42$), it is not possible to claim a purely oscillatory (sinuous) motion of the flow at $\theta = 135°$. The bend may act as a nonlinear filter yielding a more complex waveform for the flow at this plane. However, only a much lengthier (and costly) calculation could definitively resolve this.

Only one other study has discussed oscillations that occur in a developing curved-duct flow (see Tsuda and Ohba 1984; Ohba et al. 1986). The authors reported oscillations at the 90° plane in the core of the flow at $\mathrm{Re} = 1340$, but did not observe any unsteadiness at $\mathrm{Re} = 1500$. For the former case ($\mathrm{Re} = 1340$, $\mathrm{De} = 307$), the observed frequency range was approximately 0–10 Hz with a peak frequency of 3 Hz. If these values are nondimensionalized as in the present study, the peak frequency ($\omega = 0.3$) and the range ($0 \leqslant \omega \leqslant 1$) compare well with the present results at $\mathrm{Re} = 1400$, $\mathrm{De} = 541$. Differences in the dominant frequencies of the two studies may be due to differences in the measuring location and Dean number, which were significant. These differences may also explain why the authors found no low-frequency unsteadiness at the higher Reynolds number.

6. Conclusions

The laminar flow developing in a 180° curved duct has been investigated experimentally and by means of numerical simulation to yield an improved understanding of the unsteady behavior in the flow. Low-frequency oscillations of a nonturbulent nature arise in the bend for Reynolds numbers

below the critical value for unsteadiness to develop in a straight duct flow. The oscillations first occur at the outer-radius wall of the bend for streamwise positions of $90° < \theta < 180°$. In the steady-state (time-averaged) measurements, the oscillations appear as regions with artificially high RMS velocity values.

A range of frequencies can be identified. The amplitude of the oscillations varies with the distance from r_o. At positions very close to the wall ($R^* \geq 0.98$), low-frequency oscillations are damped out by viscous forces in the region. Further from the wall ($R^* = 0.95$), a single frequency or narrow band of frequencies appears to dominate the spectrum ($\omega \approx 0.09$). At the radial position furthest from r_o ($R^* = 0.92$), a broader band of frequencies appears to be important ($0.05 \leq \omega \leq 0.2$). The lowest frequency that was easily distinguishable was $\omega \approx 0.1$, equivalent to oscillations with a period of 10 time scales. Identical high-frequency harmonics were observed at both radial positions where the low-frequency oscillations were found to occur. This gives support to the idea that the source of the oscillations is the same at both radial positions.

The meandering of Goertler-type vortices, which develop in the boundary layer near r_o was identified as the probable source of the experimentally observed time-dependent behavior at Re = 1400. These vortices develop in the curved-duct flow due to the centrifugal instability in the outer-radius-wall boundary layer. The unsteadiness that develops at this Reynolds number is thought to be due to random temporal perturbations from the upstream tangent flow, which are amplified by the bend.

In simulations of the flow (both time-dependent and steady-state), the vortices appeared in the 180° bend downstream of the 135° plane. It was necessary to impose symmetry-breaking, time-dependent perturbations to visualize time-dependent behavior in the calculations. Asymmetric spatial perturbations in the calculations were insufficient to destabilize the flow field, in contrast with simulations of the fully developed flow. We conclude from this that the strong streamwise gradients that are present in the developing flow field appear to have a stabilizing influence.

As a result of the temporal perturbations imposed at the flow inlet, the vortices became unsteady, varying in their spanwise position and strength in the simulations. The fact that the Goertler-type vortices are not established until approximately the 135° plane may explain why the flow appears to remain steady in flow-visualization studies up to this position.

Acknowledgments

The authors are grateful to the reviewers for the careful reading of the manuscript and the many helpful suggestions that they gave.

References

Arnal, M. P. 1988. Investigation of developing laminar and turbulent flow in curved ducts. Ph.D. thesis, Dept. of Mechanical Engineering, University of California, Berkeley, CA

Bell, W. A. 1986. Spectral analysis of laser velocimeter data with the slotted correlation method. AIAA/ASME 4th Fluid Mechanics, Plasma Dynamics and Lasers Conference, July 13–17, 1986, Honolulu, HI, USA

Chang, S. M., Humphrey, J. A. C., and Modavi, A. 1983. Turbulent flow in a strongly curved U-bend and downstream tangent of square cross-sections. *Phys. Chem. Hydrodynam.*, **4** (3), 243

Dean, W. R. 1927. Note on the motion of fluid in a curved pipe. *Phil. Mag.*, **4**, 208

Dean, W. R. 1928a. Fluid motion in a curved channel. *Proc. R. Soc. Lond.* [*A*], **121**, 402

Dean, W. R. 1928b. The streamline motion of fluid in a curved pipe. *Phil. Mag.*, **5**, 673

Drain, L. E. 1980. *The Laser Doppler Technique*. John Wiley and Sons, New York

Goering, D. J. 1989. The influence of curvature and buoyancy in three-dimensional pipe flows. Ph.D. thesis, Dept. of Mechanical Engineering, University of California, Berkeley, CA

Hille, P., Vehrenkamp, R., and Schulz-Dubois, E. O. 1985. The development and structure of primary and secondary flow in a curved square duct. *J. Fluid Mech.*, **151**, 219

Humphrey, J. A. C. 1977. Flow in ducts with curvature and roughness. Ph.D. thesis, Mechanical Engineering Dept., London University, London, UK

Humphrey, J. A. C., Taylor, A. M. K. P., and Whitelaw, J. H. 1977. Laminar flow in a square duct of strong curvature. *J. Fluid Mech.*, **83** (3), 509

Jayanti, S. 1990. Contribution to the study of non-axisymmetric flows. Ph.D. thesis, Mechanical Engineering Dept., London University, London, UK

Johnson, R. W. and Launder, B. E. 1985. Local Nusselt number and temperature field in turbulent flow through a heated square-sectioned U-bend. *Int. J. Heat Fluid Flow*, **6** (3), 171

Ohba, K., Tsuda, N., and Takagi, K. 1986. A velocity fluctuation in developing laminar flow through a moderately curved U-bend of square cross-section. Technology Reports No. 27, Kansai University, Suita, Osaka, Japan

Patankar, S. V. 1981. *Numerical Heat Transfer and Fluid Flow*. Hemisphere, New York

Pratap, V. S. 1975. Flow and heat transfer in curved ducts. Ph.D. thesis, Mechanical Engineering Dept., London University, London, UK

Sankar, S. R., Nandakumar, K., and Masliyah, J. H. 1988. Oscillatory flows in coiled square ducts. *Phys. Fluids*, **31** (6), 1348

Schneider, G. E. and Zedan, M. 1981. A modified strongly implicit procedure for the numerical solution of field problems. *Num. Heat Trans.*, **4**, 1

Spalding, D. B. 1972. A novel finite-difference formulation for differential expressions involving both first and second derivatives. *Int. J. Num. Methods Eng.*, **4**, 551

Stone, H. L. 1968. Iterative solution of implicit approximations of multidimensional partial differential equations. *SIAM J. Numer. Anal.*, **5** (3), 530

Taylor, G. I. 1929. The criterion for turbulence in curved pipes. *Proc. R. Soc. Lond.* [*A*], **124**, 243

Tsuda, N. and Ohba, K. 1984. Laser Doppler measurement of developing laminar flow in a moderately curved U-bend of square cross-section. Second Osaka Symposium on Flow Measuring Techniques, July 13, Osaka, Japan.

Winters, K. 1987. A bifurcation study of laminar flow in a curved tube of rectangular cross-section. *J. Fluid Mech.*, **180**, 343